

Functional Map of the World

Gordon Christie¹Neil Fendley¹James Wilson²Ryan Mukherjee¹

¹The Johns Hopkins University Applied Physics Laboratory ²DigitalGlobe
 {gordon.christie, neil.fendley, ryan.mukherjee}@jhuapl.edu
 james.wilson@digitalglobe.com

Abstract

We present a new dataset, *Functional Map of the World (fMoW)*, which aims to inspire the development of machine learning models capable of predicting the functional purpose of buildings and land use from temporal sequences of satellite images and a rich set of metadata features. The metadata provided with each image enables reasoning about location, time, sun angles, physical sizes, and other features when making predictions about objects in the image. Our dataset consists of over 1 million images from over 200 countries¹. For each image, we provide at least one bounding box annotation containing one of 63 categories, including a “false detection” category. We present an analysis of the dataset along with baseline approaches that reason about metadata and temporal views. Our data, code, and pretrained models have been made publicly available.

1. Introduction

Satellite imagery presents interesting opportunities for the development of object classification methods. Most computer vision (CV) datasets for this task focus on images or videos that capture brief moments [22, 18]. With satellite imagery, temporal views of objects are available over long periods of time. In addition, metadata is also available to enable reasoning beyond visual information. For example, by combining temporal image sequences with timestamps, models may learn to differentiate office buildings from multi-unit residential buildings by observing whether or not their parking lots are full during business hours. Models may also be able to combine certain metadata parameters with observations of shadows to estimate object heights. In addition to these possibilities, robust models must be able to generalize to unseen areas around the world that may include different building materials and unique architectural styles.

Enabling the aforementioned types of reasoning requires

¹207 of the total 247 ISO Alpha-3 country codes are present in fMoW.

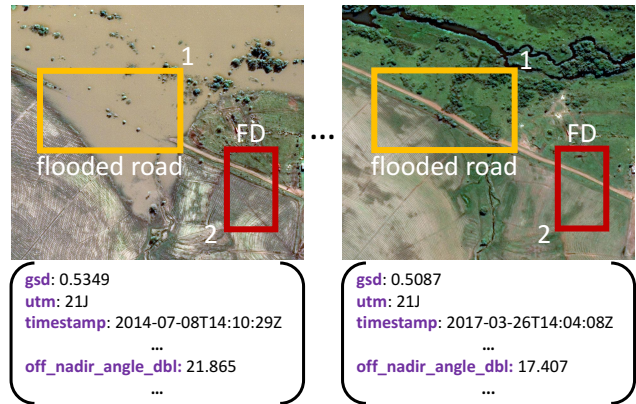


Figure 1: In fMoW, temporal sequences of images, metadata and bounding boxes for 63 categories (including “false detections”) are provided. In this example, if we only look inside the yellow box for the right image, we will only see road and vegetation. In the left image, we will only see water, and potentially predict this to be a lake. However, by observing both views of this area we can now reason that this sequence contains a flooded road.

a large dataset of annotated and geographically diverse satellite images. In this work, we present our efforts to collect such a dataset, entitled *Functional Map of the World (fMoW)*. fMoW has several notable features, including a variable number of temporal images per scene and an associated metadata file for each image. The task posed for our dataset falls in between object detection and classification. That is, for each temporal sequence of images, at least one bounding box is provided that maps to one of 63 categories, including a “false detection” (FD) category that represents content not characterized by the other 62 categories. These boxes are intended to be used as input to a classification algorithm. Figure 1 shows an example.

Collecting a dataset such as fMoW presents some interesting challenges. For example, one consideration would be to directly use crowdsourced annotations provided by OpenStreetMap² (OSM). However, issues doing so include

²<https://www.openstreetmap.org>

inconsistent, incorrect, and missing annotations for a large percentage of buildings and land use across the world. Moreover, OSM may only provide a single label for the current contents of an area, making it difficult to correctly annotate temporal views. Another possibility is to use the crowd to create annotations from scratch. However, annotating instances of a category with no prior information is extremely difficult in a large globally-diverse satellite dataset. This is due in part to the unique perspective that satellite imagery offers when compared with ground-based datasets, such as ImageNet [22]. Humans are seldom exposed to aerial viewpoints in their daily lives and, as such, objects found in satellite images tend to be visually unfamiliar and difficult to identify. Buildings can also be repurposed throughout their lifetime, making visual identification even more difficult. For these reasons, we use a multi-phase process that combines map data and crowdsourcing.

Another problem for fMoW is that full annotation is made very difficult by the increased object density for certain categories. For example, single-unit residential buildings often occur in dense clusters alongside other categories, where accurately discriminating and labeling every building would be very time-consuming. To address this shortcoming, we propose providing bounding boxes as part of algorithm input as opposed to requiring bounding box output, which would be more akin to a typical detection dataset. This avoids full image annotation issues that stem from incomplete map data and visual unfamiliarity. Imagery does not have to be fully annotated, as algorithms are only asked to classify regions with known contents. This allows us to focus collection on areas with more accurate map data and limit annotations to a small number of category instances per image.

Our contributions are summarized as follows: (1) To the best of our knowledge, we provide the largest publicly available satellite dataset containing bounding box annotations, metadata and revisits. This enables joint reasoning about images and metadata, as well as long-term temporal reasoning for areas of interest. (2) We present methods based on CNNs that exploit the novel aspects of our dataset, with performance evaluation and comparisons, which can be applied to similar problems in other application domains. Our code, data, and pretrained models have all been publicly released³. In the following sections, we provide an analysis of fMoW and baseline methods for the task.

2. Related Work

While large datasets are nothing new to the vision community, they have typically focused on first-person or ground-level imagery [22, 18, 1, 8, 9, 7, 17]. This is likely due in part to the ease with which this imagery can be col-

lected and annotated. Recently, there have been several, mostly successful, attempts to leverage techniques that were founded on first-person imagery and apply them to remote sensing data [13, 19, 28]. However, these efforts highlight the research gap that has developed due to the lack of a large dataset to appropriately characterize the problems found in remote sensing. fMoW offers an opportunity to close this gap by providing, to the best of our knowledge, the largest quantity of labeled satellite images that has been publicly released to date, while also offering several features that could help unify otherwise disparate areas of research around the multifaceted problem of processing satellite imagery. We now highlight several of these areas where we believe fMoW can make an impact.

Reasoning Beyond Visual Information Many works have extended CV research to simultaneously reason about other modules of perception, such as joint reasoning about language and vision [2, 14, 21], audio and vision [10], 2D and 3D information [3], and many others. In this work, we are interested in supporting joint reasoning about temporal sequences of images and associated metadata features. One of these features is UTM zone, which provides location context. In a similar manner, [24] shows improved image classification results by jointly reasoning about GPS coordinates and images, where several features are extracted from the coordinates, including high-level statistics about the population. Although we use coarser location features (UTM zones) than GPS in this work, we do note that using similar features would be an interesting study.

Multi-view Classification Satellite imagery offers a unique and somewhat alien perspective on the world. Most structures are designed for recognition from ground level. For example, buildings often have identifying signs above entrances that are not visible from overhead. As such, it can be difficult, if not impossible, to identify the functional purpose of a building from a single overhead image.

One of the ways in which fMoW attempts to address this issue is by providing multiple temporal views of each object, when available. Along these lines, several works in the area of video processing have been able to build upon advancements in single image classification [15, 6, 30] to create networks capable of extracting spatio-temporal features. These works may be a good starting point, but it is important to keep in mind the vastly different temporal resolution on which these datasets operate. For example, the YouTube-8M dataset [1], on which many of these video processing algorithms were developed, contains videos with 30 frames per second temporal resolution that each span on the order of minutes. Satellites, on the other hand, typically cannot capture imagery with such dense temporal resolution. Revisit times vary, but it is not uncommon for satellites to require multiple days before they can image the same location; it is possible for months to go by before they can get

³<https://github.com/fMoW>

an unobstructed view. As such, temporal views in fMoW span multiple years as opposed to minutes. Techniques that attempt to capture features across disjoint periods of time, such as [20], are likely better candidates for the task.

Perhaps the most similar work to ours in terms of temporal classification is PlaNet [26]. They pose the image localization task as a classification problem, where photos are classified as belonging to a particular bucket that bounds a specific area on the globe. They extend their approach to classify the buckets of images in photo albums taken in the same area. A similar approach is used in one of our baseline methods for fMoW.

Another recent work similar to fMoW is TorontoCity [25]. They provide a large dataset that includes imagery and LiDAR data collected by airplanes, low-altitude unmanned aerial vehicles, and cars in the greater Toronto area. While they present several tasks, the two that are related to land-use classification are zoning classification and segmentation (*e.g.*, residential, commercial). Aerial images included in TorontoCity were captured during four different years and include several seasons. While this is an impressive dataset, we believe fMoW is more focused on satellite imagery and offers advantages in geographic diversity.

Satellite Datasets One of the earliest annotated satellite datasets similar to fMoW is the UC Merced Land Use Dataset, which offers 21 categories and 100 images per category with roughly 30cm resolution and image sizes of 256x256 [29]. While some categories from this dataset overlap with fMoW, we believe fMoW offers several advantages in that we have three times the number of categories, localized objects within the images, and multiple orders of magnitude more images per category. We also provide metadata, temporal views, and multispectral images.

SpaceNet [5], a recent dataset that has received substantial attention, contains both 30cm and 50cm data of 5 cities. For the most part, the data in SpaceNet currently includes building footprints. However, earlier this year, point of interest (POI) data was also released into SpaceNet. This POI data includes the locations of several categories within Rio de Janeiro. Unrelated to SpaceNet, efforts have also been made to label data from Google Earth, with the largest released thus far being the AID [27] and NWPU-RESISC45 [4] datasets. The AID dataset includes 10,000 images of 30 categories, while the NWPU-RESISC45 dataset includes 31,500 images of 45 categories. In comparison, fMoW offers over 1,000,000 images of 63 categories. Datasets derived from Google Earth imagery lack associated metadata, temporal views, and multispectral data, which would typically be available to real-world systems.

3. Dataset Collection

Prior to the dataset collection process for fMoW, a set of categories had to be identified. Based on our target of 1

million images, collection resources, plan to collect temporal views, and discussions with researchers in the CV community, we set a goal of including between 50 and 100 categories. We searched sources such as the OSM Map Features⁴ list and NATO Geospatial Feature Concept Dictionary⁵ for categories that highlight some of the challenges discussed in Section 2. For example, “construction site” and “impoverished settlement” are categories from our dataset that may require temporal reasoning to identify, which presents a unique challenge due to temporal satellite image sequences typically being scattered across large time periods. We also focused on grouping categories according to their functional purpose, which should encourage the development of approaches that reason about contextual information, both visually and in the associated metadata.

Beyond research-based rationales for picking certain categories, we had some practical ones as well. Before categories could be annotated within images, we needed to find locations where we have high confidence of their existence. This is where maps play a crucial role. “Flooded road”, “debris or rubble”, and “construction site” were the most difficult categories to collect because open source data does not generally contain temporal information. However, with more careful search procedures, reuse of data from humanitarian response campaigns, and calculated extension of keywords to identify categories even when not directly labeled, we were able to collect temporal stacks of imagery that contained valid examples.

All imagery used in fMoW was collected from the DigitalGlobe constellation⁶. Images were gathered in pairs, consisting of 4-band or 8-band multispectral imagery in the visible to near-infrared region, as well as a pan-sharpened RGB image that represents a fusion of the high-resolution panchromatic image and the RGB bands from the lower-resolution multispectral image. 4-band imagery was obtained from either the QuickBird-2 or GeoEye-1 satellite systems, whereas 8-band imagery was obtained from WorldView-2 or WorldView-3.

More broadly, fMoW was created using a three-phase workflow consisting of location selection, image selection, and bounding box creation. The location selection phase was used to identify potential locations that map to our categories while also ensuring geographic diversity. Potential locations were drawn from several Volunteered Geographic Information (VGI) datasets, which were conflated and curated to remove duplicates. To ensure diversity, we removed neighboring locations within a specified distance (typically 500m) and set location frequency caps for categories that have severely skewed geographic distributions. These two factors helped reduce spatial density while also encouraging

⁴https://wiki.openstreetmap.org/wiki/Map_Features

⁵https://portal.dgiwg.org/files/?artifact_id=8629

⁶<https://www.digitalglobe.com/resources/satellite-information>

the selection of locations from disparate geographic areas. The remaining locations were then processed using DigitalGlobe’s GeoHIVE⁷ crowdsourcing platform. Members of the GeoHIVE crowd were asked to validate the presence of categories in satellite images, as shown in Figure 2.

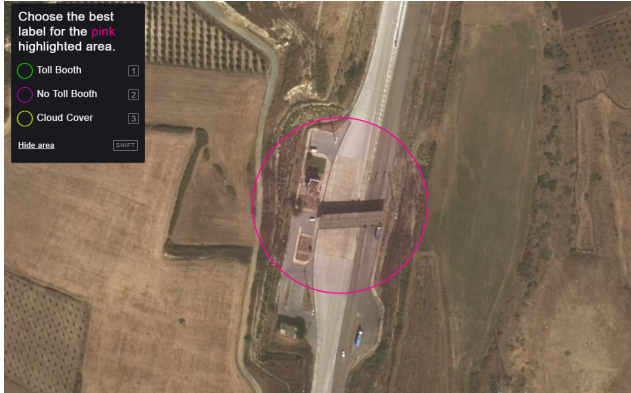


Figure 2: Sample image of what a GeoHIVE user might see while validating potential fMoW dataset features. Instructions can be seen in the top-left corner that inform users to press the ‘1’, ‘2’, or ‘3’ keys to validate existence, non-existence, or cloud obscuration of a particular object.

The image selection phase comprised of a three-step process, which included searching the DigitalGlobe satellite imagery archive, creating image chips, and filtering out cloudy images. Approximately 30% of the candidate images were removed for being too cloudy. DigitalGlobe’s IPE Data Architecture Highly-available Object-store (IDAHO) service was used to process imagery into pan-sharpened RGB and multispectral image chips in a scalable fashion. These chips were then passed through a CNN architecture to classify and remove any undesirable cloud-covered images.

Finally, images that passed through the previous two phases were sent to a curated and trusted crowd for bounding box annotation. This process involved a separate interface from the first phase, one that asked crowd users to draw bounding boxes around the category of interest in each image and provided some category-specific guidance for doing so. The resulting bounding boxes were then graded by second trusted crowd to assess quality. In total, 642 unique GeoHIVE users required a combined total of approximately 2,800 hours to annotate category instances for fMoW.

Even after multiple crowd validation procedures and implementing programmatic methods for ensuring geographic diversity, there were several categories that contained some bias. For example, the “wind farm” category does not contain very many examples from the United States, even though the initial location selection phase returned 1,938 vi-

able locations from the United States. Many of these “wind farm” instances were invalidated by the crowd, likely due to the difficulty of identifying tall, thin structures in satellite imagery, particularly when the satellite image is looking straight down on the tower. The “barn”, “construction site”, “flooded road”, and “debris or rubble” categories are also examples that contain some geographic bias. In the case of the “barn” category, the bias comes from the distribution of “barn” tags in OSM, which are predominately located in Europe, whereas the other three categories contain geographic bias as a result of the more complex feature selection process, mentioned earlier, that was required for these categories.

4. Dataset Analysis

Here we provide some statistics and analysis of fMoW. Two versions of the dataset are publicly available:

- **fMoW-full** The full version of the dataset includes pan-sharpened RGB images and 4/8-band multispectral images (MSI), which are both stored in TIFF format. Pan-sharpened images are created by “sharpening” lower-resolution MSI using higher-resolution panchromatic imagery. All pan-sharpened images in **fMoW-full** have corresponding MSI, where the metadata files for these images are nearly identical.
- **fMoW-rgb** An alternative JPEG compressed version of the dataset, which is provided since **fMoW-full** is very large. For each pan-sharpened RGB image we simply perform a conversion to JPEG. For MSI images, we extract the RGB channels and save them as JPEGs.

For all experiments presented in this paper, we use **fMoW-rgb**. We also exclude RGB-extracted versions of the MSI in **fMoW-rgb** as they are effectively downsampled versions of the pan-sharpened RGB images.

4.1. fMoW Splits

We have made the following splits to the dataset:

- **seq** This is the sequestered portion of the dataset that is not currently publicly available. It will be released after it is used for final testing in the public challenge centered around the dataset⁸.
- **train** Contains 65.2% and 72.13% of the total bounding boxes with and without **seq** included, respectively.
- **val** Contains 11.4% and 12.6% of the total bounding boxes with and without **seq** included, respectively. This set was made representative of **test**, so that validation can be performed.
- **test** Contains 13.8% and 15.3% of the total bounding boxes with and without **seq** included, respectively.

⁷<https://geohive.digitalglobe.com>

⁸<https://www.iarpa.gov/challenges/fmow.html>

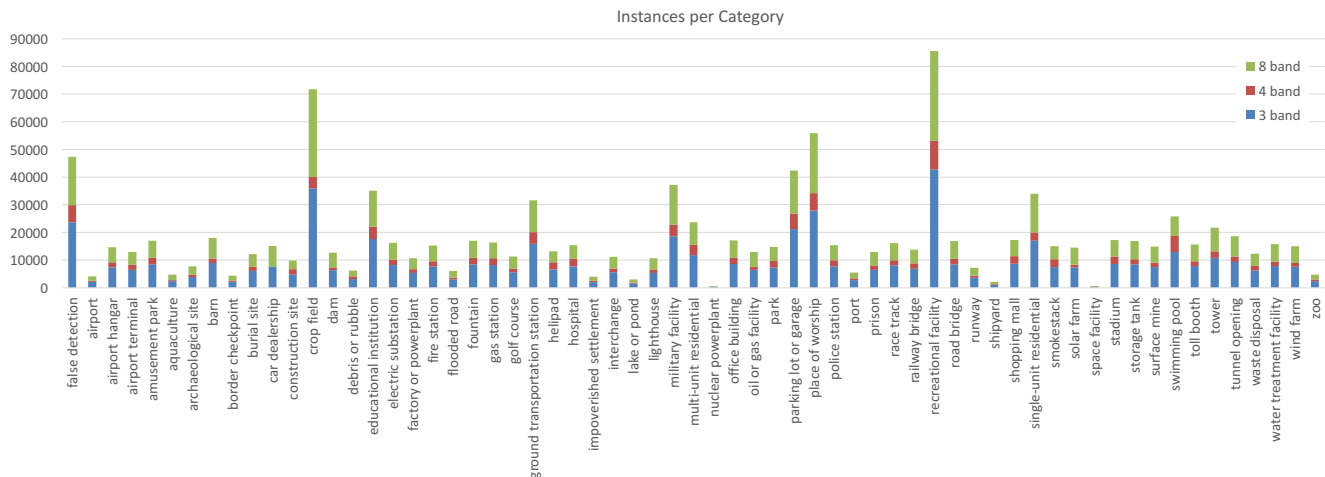


Figure 3: This shows the total number of instances for each category (including FD) in fMoW across different number of bands. These numbers include the temporal views of the same areas. `fMoW-full` consists of 3 band imagery (pan-sharpened RGB), as well as 4 and 8 band imagery. In `fMoW-rgb`, the RGB channels of the 4 and 8 band imagery are extracted and saved as JPEG images.

The total number of bounding box instances for each category can be seen in Figure 3.

4.2. fMoW Statistics

Variable length sequences of images are provided for each scene in the dataset. Figure 4 shows what percentage of the sequences in the dataset belong to each sequence length. 21.2% of the sequences contain only 1 view. Most (95%) of the sequences contain 10 or less images.

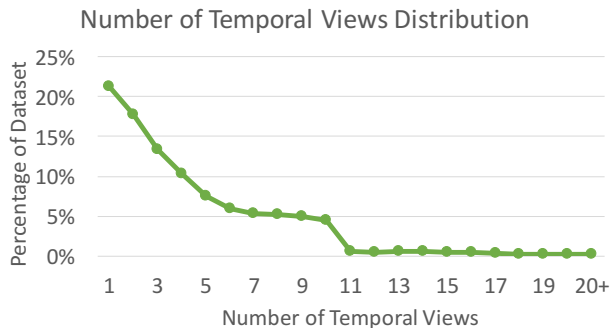


Figure 4: This shows the distribution of the number of temporal views in our dataset. The number of temporal views is not incremented by both the pan-sharpened and multispectral images. These images have almost identical metadata files and are therefore not counted twice. The maximum number of temporal views for any area in the dataset is 41.

A major focus of the collection effort was global diversity. In the metadata, we provide UTM zones, which typically refer to 6° longitude bands (1-60). We also concatenate letters that represent latitude bands (total of 20) to the

UTM zones in the metadata. Figure 5 illustrates the frequency of sequences within the UTM zones on earth, where the filled rectangles each represent a different UTM zone. Green colors represent areas with higher numbers of sequences, while blue regions have lower counts. As seen, fMoW covers much of the globe. The images captured for fMoW also have a wide range of dates, which allows algorithms to analyze areas on earth over long periods of time in some cases. Figure 6 shows a distributions for years and local times (converted from UTC) in which the images were captured. The average time difference between the earliest and most recent images in each sequence is approximately 3.8 years.

5. Baselines and Methods

Here we present 5 different approaches to our task, which vary by their use of metadata and temporal reasoning. All experiments were performed using `fMoW-rgb`. Two of the methods presented involve fusing metadata into a CNN architecture. The following provides a summary of the metadata features that are used, as well as any preprocessing operations that are applied:

- **UTM Zone** One of 60 UTM zones and one of 20 latitude bands are combined for this feature. We convert these values to 2 coordinate values, each between 0 and 1. This is done by taking the indices of the values within the list of possible values and then normalizing.
- **Timestamp** The year, month, day, hour, minute, second, and day of the week are extracted from the timestamp and added as separate features. The timestamp provided in the metadata files is in Coordinated Universal Time (UTC).

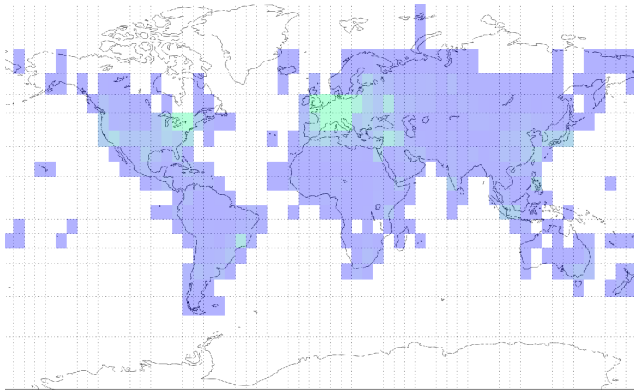


Figure 5: This shows the geographic diversity of fMoW. Data was collected from over 400 unique UTM zones (including latitude bands). This helps illustrate the number of images captured in each UTM zone, where more green colors show UTM zones with a higher number of instances, and more blue colors show UTM zones with lower counts.

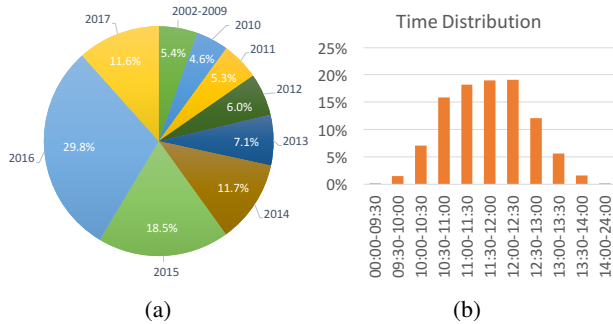


Figure 6: Distribution over (a) years the images were captured, and (b) time of day the images were captured (UTC converted to local time for this figure).

- **GSD** Ground sample distance, measured in meters, is provided for both the panchromatic and multispectral bands in the image strip. The panchromatic images used to generate the pan-sharpened RGB images have higher resolution than the MSI, and therefore have smaller GSD values. These GSD values, which describe the physical sizes of pixels in the image, are used directly without any preprocessing.
- **Angles** These identify the angle at which the sensor is imaging the ground, as well as the angular location of the sun with respect to the ground and image. These features can be added without preprocessing. The following angles are provided:
 - *Off-nadir Angle* Angle in degrees (0-90°) between the point on the ground directly below the sensor and the center of the image swath.
 - *Target Azimuth* Angle in degrees (0-360°) of clockwise rotation off north to the image swath’s

major axis.

- *Sun Azimuth* Angle in degrees (0-360°) of clockwise rotation off north to the sun.
- *Sun Elevation* Angle in degrees (0-90°) of elevation, measured from the horizontal, to the sun.
- **Image+box sizes** The pixel dimensions of the bounding boxes and image size, as well as the fraction of the image width and height that the boxes occupy are added as features.

After preprocessing the metadata features, we perform mean subtraction and normalization using values calculated for `train+val`. A full list of metadata features and their descriptions can be found in the appendix.

It is worth noting here that the imagery in fMoW is not registered, and while many sequences have strong spatial correspondence, individual pixel coordinates in different images do not necessarily represent the same positions on the ground. As such, we are prevented from easily using methods that exploit registered sequences.

The CNN used as the base model in our various baseline methods is DenseNet-161 [12], with 48 feature maps ($k=48$). During initial testing, we found this model to outperform other models such as VGG-16 [23] and ResNet-50 [11]. We initialize our base CNN models using the pre-trained ImageNet weights, which we found to improve performance during initial tests. Training is performed using a crop size of 224x224, the Adam optimizer [16], and an initial learning rate of $1e-4$. Due to class imbalance in our dataset, we attempted to weight the loss using class frequencies, but did not observe any improvement.

To merge metadata features into the model, the softmax layer of DenseNet is removed and replaced with a concatenation layer to merge DenseNet features with preprocessed metadata features, followed by two 4096-d fully-connected layers with 50% dropout layers, and a softmax layer with 63 outputs (62 main categories + FD). An illustration of this base model is shown in Figure 7.

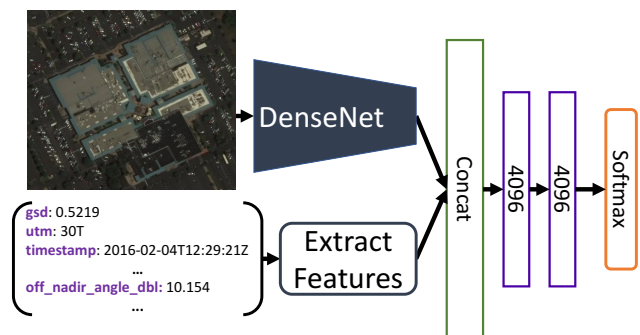


Figure 7: An illustration of our base model used to fuse metadata features into the CNN. This model is used as a baseline and also as a feature extractor (without softmax) for providing features to an LSTM. Dropout layers are added after the 4096-d FC layers.

We test the following approaches with fMoW:

- **LSTM-M** An LSTM architecture trained using temporal sequences of metadata features. We believe training solely on metadata helps understand how important images are in making predictions, while also providing some measure of bias present in fMoW.
- **CNN-I** A standard CNN approach using only images, where DenseNet is fine-tuned after ImageNet. Softmax outputs are summed over each temporal view, after which an argmax is used to make the final prediction. The CNN is trained on all images across all temporal sequences of `train + val`.
- **CNN-IM** A similar approach to CNN-I, but with metadata features concatenated to the features of DenseNet before the fully connected layers.
- **LSTM-I** An LSTM architecture trained using features extracted from CNN-I.
- **LSTM-IM** An LSTM architecture trained using features extracted from CNN-IM.

All of these methods are trained on `train + val`. Since tight bounding boxes are typically provided for category instances in the dataset, we add a context buffer around each box before extracting the region of interest from the image. We found that it was useful to provide more context for categories with smaller sizes (*e.g.*, single-unit residential) and less context for categories that generally cover larger areas (*e.g.*, airports).

Per-category F1 scores for `test` are shown in Table 1. From the results, it can be observed that, in general, the LSTM architectures show similar performance to our approaches that sum the probabilities over each view. Some possible contributors to this are the large quantity of single-view images provided in the dataset, and that temporal changes may not be particularly important for several of the categories. CNN-I and CNN-IM are also, to some extent, already reasoning about temporal information while making predictions by summing the softmax outputs over each temporal view. Qualitative results that show success and failure cases for LSTM-I are shown in Figure 8. Qualitative results are not shown for the approaches that use metadata, as it is much harder to visually show why the methods succeed in most cases.

It could be argued that the results for approaches using metadata are only making improvements because of bias exploitation. To show that metadata helps beyond inherent bias, we removed all instances from the test set where the metadata-only baseline (LSTM-M) is able to correctly predict the category. The results of this removal, which can be found in Table 2, show that metadata can still be useful for improving performance.

To further confirm the importance of temporal reasoning, we compare the methods presented above with two additional methods, CNN-I-1 and CNN-IM-1, which make

	LSTM-M	CNN-I	LSTM-I	CNN-IM	LSTM-IM
false_detection	0.599	0.728	0.729	0.853	0.837
airport	0.447	0.859	0.800	0.884	0.837
airport hangar	0.017	0.721	0.665	0.677	0.699
airport terminal	0.023	0.697	0.715	0.746	0.759
amusement park	0.622	0.746	0.727	0.898	0.868
aquaculture	0.514	0.754	0.762	0.811	0.805
archaeological site	0.016	0.524	0.491	0.574	0.607
barn	0.292	0.695	0.684	0.717	0.707
border checkpoint	0.000	0.333	0.404	0.523	0.515
burial site	0.019	0.852	0.859	0.827	0.846
car dealership	0.101	0.741	0.797	0.747	0.770
construction site	0.053	0.372	0.373	0.318	0.358
crop field	0.514	0.888	0.872	0.930	0.926
dam	0.158	0.806	0.798	0.864	0.886
debris or rubble	0.381	0.403	0.607	0.474	0.488
educational institution	0.157	0.495	0.475	0.548	0.557
electric substation	0.000	0.849	0.869	0.858	0.872
factory or powerplant	0.000	0.443	0.459	0.536	0.544
fire station	0.028	0.409	0.494	0.483	0.523
flooded road	0.625	0.296	0.285	0.638	0.795
fountain	0.085	0.727	0.705	0.814	0.840
gas station	0.022	0.785	0.779	0.761	0.772
golf course	0.220	0.860	0.916	0.899	0.875
ground transportation station	0.114	0.658	0.694	0.713	0.719
helipad	0.067	0.812	0.856	0.831	0.820
hospital	0.012	0.387	0.404	0.426	0.458
impoverished settlement	0.538	0.410	0.506	0.750	0.704
interchange	0.142	0.833	0.678	0.905	0.909
lake or pond	0.000	0.721	0.650	0.687	0.694
lighthouse	0.037	0.715	0.755	0.779	0.828
military facility	0.426	0.509	0.564	0.597	0.655
multi-unit residential	0.227	0.385	0.414	0.445	0.451
nuclear powerplant	0.000	0.720	0.762	0.600	0.552
office building	0.011	0.198	0.218	0.228	0.225
oil or gas facility	0.522	0.789	0.773	0.844	0.865
park	0.025	0.626	0.638	0.662	0.698
parking lot or garage	0.076	0.775	0.787	0.700	0.732
place of worship	0.362	0.638	0.658	0.712	0.735
police station	0.068	0.246	0.237	0.201	0.329
port	0.444	0.692	0.698	0.736	0.667
prison	0.087	0.611	0.650	0.695	0.726
race track	0.234	0.898	0.886	0.919	0.892
railway bridge	0.030	0.703	0.755	0.761	0.813
recreational facility	0.295	0.907	0.919	0.903	0.906
road bridge	0.000	0.722	0.738	0.747	0.756
runway	0.488	0.821	0.814	0.889	0.885
shipyard	0.000	0.371	0.351	0.368	0.351
shopping mall	0.117	0.615	0.629	0.662	0.662
single-unit residential	0.429	0.688	0.703	0.717	0.684
smokestack	0.204	0.735	0.755	0.772	0.768
solar farm	0.424	0.912	0.921	0.927	0.931
space facility	0.000	0.824	0.737	0.875	0.889
stadium	0.174	0.825	0.850	0.818	0.819
storage tank	0.140	0.921	0.921	0.928	0.924
surface mine	0.200	0.824	0.802	0.870	0.880
swimming pool	0.362	0.920	0.913	0.906	0.907
toll booth	0.030	0.891	0.918	0.960	0.954
tower	0.141	0.723	0.737	0.754	0.777
tunnel opening	0.526	0.867	0.897	0.949	0.942
waste disposal	0.071	0.595	0.570	0.604	0.670
water treatment facility	0.044	0.854	0.816	0.853	0.879
wind farm	0.540	0.939	0.948	0.959	0.968
zoo	0.039	0.566	0.582	0.598	0.611
Average	0.193	0.679	0.688	0.722	0.734

Table 1: F1 scores for different approaches on `test`. Color formatting was applied to each column independently. The average values shown at the bottom of the table are calculated without FD scores.

predictions for each individual view. We then have all other methods repeat their prediction over the full sequence. This is done to show that, on average, seeing an area multiple times outperforms single-view predictions. We note that these tests are clearly not fair for some categories, such as

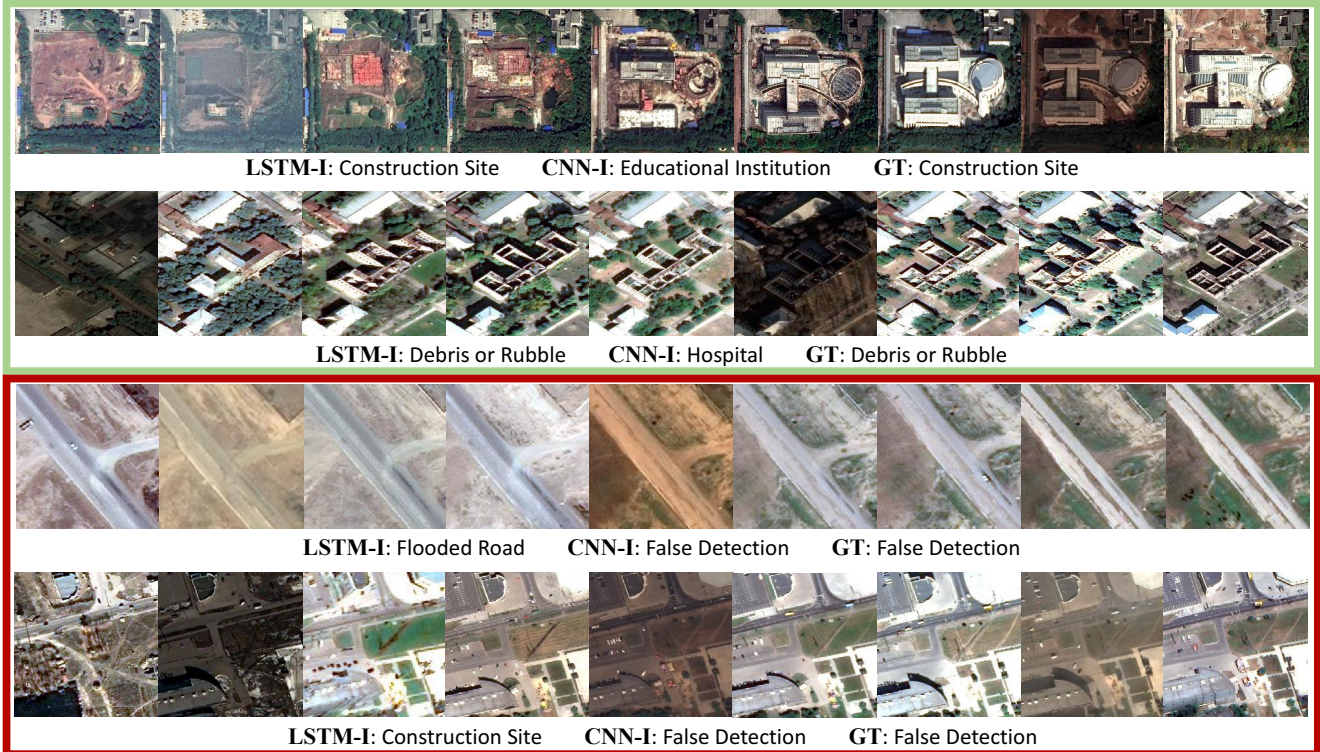


Figure 8: Qualitative examples from `test` of the image-only approaches. The images presented here show the extracted and resized images that are passed to the CNN approaches. The top two rows show success cases for LSTM-I, where CNN-I was not able to correctly predict the category. The bottom two rows show failure cases for LSTM-I, where CNN-I was able to correctly predict the category. We also note that sequences with ≥ 9 views were chosen. The second row was trimmed to keep the figure consistent. However, we note that variable temporal views are provided for throughout the dataset.

“construction site”, where some views may not even contain the category. However, we perform these tests for completeness to confirm our expectations. Results are shown in Table 3. Per-category results can be found in the appendix.

LSTM-M	CNN-I	LSTM-I	CNN-IM	LSTM-IM
0	0.685	0.693	0.695	0.702

Table 2: Results on `test` instances where the metadata-only baseline (LSTM-M) is not able to correctly predict the category. These are the average F1 scores not including FD. These results show that metadata is important beyond exploiting bias in the dataset.

CNN-I-1	CNN-I	LSTM-I	CNN-IM-1	CNN-IM	LSTM-IM
0.618	0.678	0.684	0.666	0.722	0.735

Table 3: Average F1 scores, not including FD, for individual images from `test`. CNN-I-1 and CNN-IM-1 make predictions for each individual view. All other methods repeat their prediction over the full sequence.

6. Conclusion and Discussion

We present fMoW, a dataset that consists of over 1 million image and metadata pairs, of which many are temporal views of the same scene. This enables reasoning beyond visual information, as models are able to leverage temporal information and reason about the rich set of metadata features (*e.g.*, timestamp, UTM zone) provided for each image. By posing a task in between detection and classification, we avoid the inherent challenges associated with collecting a large, geographically diverse, detection dataset, while still allowing for models to be trained that are transferable to real-world detection systems. Different methods were presented for this task that demonstrate the importance of reasoning about metadata and temporal information. All code, data, and pretrained models have been made publicly available. We hope that by releasing the dataset and code, other researchers in the CV community will find new and interesting ways to further utilize the metadata and temporal changes to a scene. We also hope to see fMoW being used to train models that are able to assist in humanitarian efforts, such as applications involving disaster relief.

Acknowledgements This work would not have been possible without the help of everyone on the fMoW Challenge team, who we thank for their contributions. A special thanks to: Kyle Ellis, Todd Bacastow, Alex Dunmire, and Derick Greyling from DigitalGlobe; Rebecca Allegar, Jillian Brennan, Dan Reitz, and Ian Snyder from Booz Allen Hamilton; Kyle Bowerman and Gódehy Balázs from Topcoder; and, finally, Myron Brown, Philippe Burlina, Alfred Mayalu, and Nicolas Norena Acosta from JHU/APL. We also thank the professors, graduate students, and researchers in industry and from the CV community for their suggestions and participation in discussions that helped shape the direction of this work.

The material in this paper is based upon work supported by the Office of the Director of National Intelligence (ODNI), Intelligence Advanced Research Projects Activity (IARPA), via Contract 2017-17032700004. The views and conclusions contained herein are those of the authors and should not be interpreted as necessarily representing the official policies or endorsements, either expressed or implied, of the ODNI, IARPA, or the U.S. Government. The U.S. Government is authorized to reproduce and distribute reprints for Governmental purposes notwithstanding any copyright annotation therein.

Appendix Overview

In this document, we provide:

- Appendix I: Descriptions of the metadata features and distributions for country codes and UTM zones.
- Appendix II: Additional collection details.
- Appendix III: Additional results.
- Appendix IV: Examples from our dataset.

Appendix I. Metadata Features and Statistics

1. **ISO Country Code** ISO Alpha-3 country code (String). There are a total of 247 possible country codes, 207 of which are present in fMoW.
2. **UTM Zone** Universal Transverse Mercator. There are 60 UTM zones, which are 6° in width. We provide a number for the UTM zone (1-60), along with a letter representing the latitude band. There are a total of 20 latitude bands, which range from “C” to “X” (“I” and “O” are not included).
3. **Timestamp** UTC timestamp. Datetime format (Python): “%Y-%m-%dT%H:%M:%SZ” (String).
4. **Cloud Cover** Fraction of the image strip, not image chip, that is completely obscured by clouds on a scale of 0-100 (Integer).
5. **Scan Direction** The direction the sensor is pointed when collecting an image strip. Either “Forward”, when the image is collected ahead of the orbital path or “Reverse” when the image is taken behind the orbital path (String).
6. **Pan Resolution** Ground sample distance of panchromatic band (pan-GSD) in the image strip, measured in meters (Double). `start`, `end`, `min`, and `max` values are also included. `start` and `end` represent the pan-GSD for the first and last scan lines, respectively. `min` and `max` represent the minimum and maximum pan-GSD for all scan lines, respectively.
7. **Multi Resolution** Ground sample distance of multi-spectral bands (multi-GSD) in the image strip, measured in meters (Double). `start`, `end`, `min`, and `max` values are also included. `start` and `end` represent the multi-GSD for the first and last scan lines, respectively. `min` and `max` represent the minimum and maximum multi-GSD for all scan lines, respectively.
8. **Target Azimuth** Azimuth angle of the sensor with respect to the center of the image strip, measured in degrees (Double). `start`, `end`, `min`, and `max` values are also included. `start` and `end` represent the target azimuth for the first and last scan lines, respectively. `min` and `max` represent the minimum and maximum target azimuth for all scan lines, respectively.
9. **Sun Azimuth** Azimuth angle of the sun measured from north, clockwise in degrees, to the center of the image strip, measured in degrees (Double). `min` and `max` values are also included. `min` and `max` represent the minimum and maximum sun azimuth for all scan lines, respectively.
10. **Sun Elevation** Elevation angle of the sun measured from the horizontal, measured in degrees (Double). `min` and `max` values are also included. `min` and `max` represent the minimum and maximum sun elevation for all scan lines, respectively.
11. **Off-Nadir Angle** The off nadir angle of the satellite with respect to the center of the image strip, measured in degrees (Double). `start`, `end`, `min`, and `max` values are also included. `start` and `end` represent the off-nadir angle for the first and last scan lines, respectively. `min` and `max` represent the minimum and maximum off-nadir angle for all scan lines, respectively.

Country Codes Here we show the counts for each unique country code in fMoW. Counts are incremented once for each sequence instead of once per metadata file.

[(“USA”, 18750), (“FRA”, 7470), (“ITA”, 6985), (“RUS”, 6913), (“CHN”, 6597), (“DEU”, 4686), (“GBR”, 4496), (“BRA”, 3820), (“CAN”, 3128), (“TUR”, 2837), (“JPN”, 2542), (“IDN”, 2448), (“ESP”, 2402), (“AUS”, 2105), (“DZA”, 1849), (“IND”, 1804), (“UKR”, 1735), (“CZE”, 1713), (“POL”, 1386), (“MEX”, 1274), (“ARG”, 1248), (“NLD”, 1236), (“SYR”, 1224), (“BEL”, 1190), (“PHL”, 1179), (“IRQ”, 1129), (“EGY”, 1041), (“ZAF”, 924), (“CHL”, 888), (“LTU”, 871), (“LBY”, 863), (“KOR”, 809), (“CHE”, 788), (“LVA”, 772), (“PRT”, 722), (“YEM”,

701), (“BLR”, 601), (“GRC”, 592), (“AUT”, 572), (“SVN”, 570), (“ARE”, 566), (“IRN”, 540), (“COL”, 509), (“TWN”, 509), (“TZA”, 475), (“NZL”, 465), (“PER”, 459), (“HTI”, 417), (“KEN”, 405), (“NGA”, 383), (“VEN”, 378), (“PRK”, 371), (“ECU”, 351), (“IRL”, 335), (“MYS”, 328), (“BOL”, 313), (“FIN”, 288), (“KAZ”, 268), (“MAR”, 266), (“TUN”, 257), (“CUB”, 256), (“EST”, 247), (“SAU”, 246), (“HUN”, 222), (“THA”, 219), (“NPL”, 196), (“HRV”, 187), (“NOR”, 183), (“SVK”, 175), (“SEN”, 172), (“BGD”, 171), (“HND”, 167), (“SWE”, 166), (“BGR”, 165), (“HKG”, 154), (“DNK”, 153), (“MDA”, 147), (“ROU”, 142), (“ZWE”, 141), (“SRB”, 140), (“GTM”, 140), (“DOM”, 134), (“LUX”, 133), (“SDN”, 132), (“VNM”, 126), (“URY”, 120), (“CRI”, 119), (“SOM”, 112), (“ISL”, 110), (“LKA”, 110), (“QAT”, 108), (“PRY”, 107), (“SGP”, 106), (“OMN”, 105), (“PRI”, 95), (“NIC”, 87), (“NER”, 85), (“SSD”, 82), (“UGA”, 79), (“SLV”, 79), (“JOR”, 78), (“CMR”, 77), (“PAN”, 74), (“PAK”, 72), (“UZB”, 70), (“CYP”, 67), (“KWT”, 67), (“ALB”, 66), (“CIV”, 65), (“BHR”, 65), (“GIN”, 64), (“MLT”, 63), (“JAM”, 62), (“AZE”, 62), (“GEO”, 60), (“SLE”, 59), (“ETH”, 58), (“LBN”, 57), (“ZMB”, 55), (“TTO”, 54), (“LBR”, 52), (“BWA”, 51), (“ANT”, 50), (“BHS”, 50), (“MNG”, 46), (“MKD”, 45), (“GLP”, 45), (“COD”, 45), (“KO-”, 42), (“BEN”, 42), (“GHA”, 41), (“MDG”, 36), (“MLI”, 35), (“AFG”, 35), (“ARM”, 33), (“MRT”, 33), (“KHM”, 32), (“CPV”, 31), (“TKM”, 31), (“MMR”, 31), (“BFA”, 29), (“BLZ”, 29), (“NCL”, 28), (“AGO”, 27), (“FJI”, 26), (“TCD”, 25), (“MTQ”, 25), (“GMB”, 23), (“SWZ”, 23), (“BIH”, 21), (“CAF”, 19), (“GUF”, 19), (“PSE”, 19), (“MOZ”, 18), (“NAM”, 18), (“SUR”, 17), (“GAB”, 17), (“LSO”, 16), (“ERI”, 15), (“BRN”, 14), (“REU”, 14), (“GUY”, 14), (“MAC”, 13), (“TON”, 13), (“ABW”, 12), (“PYF”, 12), (“TGO”, 12), (“BRB”, 12), (“VIR”, 11), (“CA-”, 11), (“DJI”, 11), (“FLK”, 11), (“MNE”, 11), (“KGZ”, 11), (“ESH”, 10), (“LCA”, 10), (“BMU”, 10), (“COG”, 9), (“ATG”, 9), (“BDI”, 9), (“GIB”, 8), (“LAO”, 8), (“GNB”, 8), (“DMA”, 8), (“KNA”, 8), (“GNQ”, 7), (“RWA”, 7), (“BTN”, 7), (“TJK”, 6), (“TCA”, 5), (“VCT”, 4), (“WSM”, 3), (“IOT”, 3), (“AND”, 3), (“ISR”, 3), (“AIA”, 3), (“MDV”, 2), (“SHN”, 2), (“VGB”, 2), (“MSR”, 2), (“PNG”, 1), (“MHL”, 1), (“VUT”, 1), (“GRD”, 1), (“VAT”, 1), (“MCO”, 1)]

UTM Zones Here we show the counts for each unique UTM zone in fMoW. Counts are incremented once for each sequence instead of once per metadata file.

[(“31U”, 5802), (“32T”, 4524), (“33T”, 4403), (“30U”, 4186), (“32U”, 3864), (“33U”, 3315), (“31T”, 3150), (“18T”, 2672), (“17T”, 2339), (“34U”, 2049), (“37S”, 1718), (“30T”, 1686), (“37U”, 1672), (“23K”, 1627), (“18S”, 1481), (“11S”, 1388), (“16T”, 1283), (“54S”, 1244), (“38S”, 1229), (“31S”, 1227), (“35U”, 1137), (“35V”, 1116), (“52S”, 1115), (“16S”, 1110), (“51P”,

1086), (“51R”, 1069), (“36S”, 1046), (“35T”, 1038), (“36R”, 1037), (“49M”, 1026), (“48M”, 1021), (“10T”, 1010), (“53S”, 1001), (“10S”, 955), (“14R”, 935), (“19T”, 928), (“30S”, 912), (“17S”, 875), (“17R”, 874), (“43P”, 854), (“50S”, 796), (“36U”, 767), (“50R”, 751), (“33S”, 751), (“32S”, 746), (“14S”, 730), (“34T”, 728), (“12S”, 716), (“37M”, 705), (“13S”, 676), (“37T”, 667), (“36T”, 653), (“15S”, 629), (“55H”, 618), (“34S”, 604), (“29S”, 600), (“38P”, 598), (“15T”, 586), (“22J”, 585), (“18Q”, 549), (“15R”, 539), (“35S”, 511), (“10U”, 497), (“21H”, 492), (“36V”, 491), (“19H”, 482), (“48R”, 476), (“49S”, 459), (“48S”, 446), (“49Q”, 444), (“29T”, 438), (“16P”, 429), (“56H”, 425), (“14Q”, 422), (“40R”, 420), (“39R”, 413), (“39U”, 406), (“18N”, 385), (“35J”, 383), (“37V”, 380), (“50T”, 379), (“56J”, 355), (“34V”, 351), (“43V”, 347), (“29U”, 346), (“38U”, 345), (“17M”, 328), (“38T”, 323), (“19P”, 323), (“51S”, 317), (“54H”, 311), (“49R”, 295), (“34H”, 293), (“22K”, 293), (“48N”, 276), (“20H”, 273), (“50Q”, 268), (“28P”, 262), (“18L”, 260), (“24M”, 258), (“24L”, 256), (“21J”, 255), (“41V”, 254), (“13T”, 254), (“47N”, 253), (“40U”, 253), (“45R”, 251), (“43Q”, 245), (“51Q”, 243), (“51T”, 240), (“39S”, 239), (“19K”, 238), (“19Q”, 237), (“59G”, 236), (“43R”, 234), (“12T”, 230), (“49T”, 227), (“41U”, 223), (“32V”, 219), (“30V”, 212), (“13Q”, 212), (“40V”, 210), (“16R”, 210), (“20T”, 210), (“38R”, 204), (“36J”, 203), (“46T”, 200), (“45T”, 197), (“44U”, 196), (“15Q”, 190), (“50L”, 190), (“32P”, 184), (“60H”, 182), (“47P”, 182), (“20P”, 181), (“24K”, 178), (“17Q”, 178), (“35K”, 169), (“20J”, 168), (“11U”, 165), (“18H”, 164), (“52T”, 163), (“11T”, 161), (“36N”, 158), (“39V”, 157), (“20K”, 157), (“39Q”, 155), (“12U”, 149), (“38V”, 147), (“18P”, 147), (“23L”, 147), (“18G”, 146), (“31N”, 146), (“19J”, 142), (“33P”, 141), (“40Q”, 136), (“13R”, 136), (“47T”, 132), (“47R”, 126), (“48U”, 124), (“32R”, 123), (“15P”, 121), (“39P”, 117), (“48P”, 117), (“33R”, 116), (“45U”, 113), (“43S”, 111), (“44N”, 109), (“54T”, 109), (“32N”, 109), (“36W”, 108), (“17P”, 108), (“36P”, 105), (“31R”, 104), (“56K”, 101), (“20Q”, 101), (“39T”, 97), (“16Q”, 96), (“29R”, 95), (“25L”, 92), (“45Q”, 91), (“46Q”, 91), (“48T”, 90), (“44Q”, 89), (“42V”, 87), (“29N”, 87), (“43U”, 86), (“4Q”, 86), (“47Q”, 85), (“48Q”, 84), (“30N”, 83), (“19G”, 82), (“25M”, 81), (“42Q”, 80), (“44P”, 80), (“20L”, 77), (“50J”, 77), (“53U”, 76), (“38N”, 75), (“27W”, 75), (“44R”, 75), (“33V”, 74), (“34R”, 72), (“49L”, 70), (“36M”, 69), (“40S”, 69), (“12R”, 68), (“37P”, 68), (“52R”, 65), (“14T”, 64), (“50U”, 62), (“35H”, 62), (“50H”, 61), (“28R”, 60), (“54U”, 59), (“46V”, 58), (“44T”, 56), (“21K”, 56), (“55G”, 56), (“22L”, 56), (“35P”, 55), (“31P”, 54), (“29P”, 54), (“35R”, 52), (“30R”, 51), (“19U”, 50), (“53T”, 49), (“46U”, 49), (“50N”, 48), (“47S”, 48), (“42R”, 48), (“37Q”, 47), (“19L”, 47), (“14U”, 47), (“28Q”, 46), (“37N”, 45), (“19F”, 45), (“42U”, 44), (“36K”, 42), (“37R”, 40), (“37W”, 40),

(“41S”, 38), (“42S”, 38), (“38Q”, 37), (“30P”, 37), (“42T”, 36), (“35L”, 36), (“46R”, 36), (“52U”, 35), (“60G”, 35), (“27V”, 34), (“45V”, 34), (“35W”, 34), (“13U”, 34), (“35M”, 34), (“18M”, 32), (“17L”, 32), (“41W”, 32), (“17N”, 31), (“21N”, 31), (“23M”, 30), (“21L”, 29), (“28S”, 28), (“58K”, 28), (“22M”, 28), (“41R”, 27), (“18R”, 27), (“10V”, 26), (“57U”, 26), (“34K”, 26), (“49U”, 25), (“6V”, 25), (“38L”, 25), (“20G”, 25), (“33L”, 24), (“60K”, 24), (“55K”, 23), (“51N”, 23), (“22H”, 22), (“22N”, 22), (“47V”, 22), (“41T”, 21), (“44V”, 21), (“36Q”, 21), (“46S”, 20), (“22T”, 20), (“34N”, 19), (“20U”, 19), (“12Q”, 19), (“12V”, 19), (“19N”, 18), (“31Q”, 18), (“21M”, 18), (“52L”, 18), (“56V”, 18), (“52V”, 18), (“23J”, 16), (“45W”, 16), (“9U”, 16), (“34J”, 16), (“27P”, 16), (“43W”, 15), (“1K”, 14), (“33M”, 14), (“40W”, 14), (“40K”, 14), (“43T”, 14), (“55T”, 14), (“51U”, 13), (“53K”, 13), (“34M”, 13), (“32M”, 13), (“37L”, 13), (“21P”, 12), (“50P”, 12), (“35N”, 12), (“6K”, 11), (“59H”, 11), (“33K”, 11), (“20M”, 11), (“49N”, 11), (“5Q”, 10), (“6W”, 10), (“26Q”, 10), (“39L”, 10), (“47U”, 10), (“34W”, 10), (“50K”, 10), (“8V”, 10), (“20S”, 10), (“40T”, 9), (“51V”, 9), (“42W”, 8), (“60W”, 8), (“53H”, 8), (“50V”, 8), (“20F”, 8), (“53L”, 7), (“18F”, 7), (“35Q”, 7), (“30Q”, 7), (“44S”, 7), (“15M”, 7), (“5V”, 7), (“54J”, 7), (“39W”, 6), (“49P”, 6), (“50M”, 6), (“19V”, 6), (“21F”, 6), (“20N”, 5), (“14P”, 5), (“34P”, 5), (“53J”, 5), (“38M”, 5), (“51K”, 5), (“29Q”, 4), (“11R”, 4), (“49V”, 4), (“48V”, 4), (“51M”, 4), (“38W”, 4), (“33N”, 4), (“45S”, 4), (“27Q”, 4), (“55J”, 3), (“19M”, 3), (“53V”, 3), (“2W”, 3), (“32Q”, 3), (“2L”, 3), (“16M”, 3), (“57W”, 3), (“43M”, 3), (“53W”, 2), (“43N”, 2), (“52J”, 2), (“28M”, 2), (“56T”, 2), (“33H”, 2), (“21T”, 2), (“44W”, 2), (“15V”, 1), (“33W”, 1), (“60V”, 1), (“18K”, 1), (“31M”, 1), (“54M”, 1), (“58P”, 1), (“58W”, 1), (“40X”, 1), (“58G”, 1), (“57V”, 1), (“16U”, 1), (“59K”, 1), (“52N”, 1), (“2K”, 1), (“33Q”, 1), (“34Q”, 1), (“11V”, 1), (“56W”, 1), (“26P”, 1), (“28W”, 1), (“59W”, 1), (“38K”, 1), (“26S”, 1), (“7L”, 1), (“56U”, 1), (“55V”, 1)]

Appendix II. Dataset Collection

The location selection phase was used to identify potential locations that map to our categories while also ensuring geographic diversity. Potential locations were drawn from several Volunteered Geographic Information (VGI) datasets, which were conflated and curated to remove duplicates and ensure geographic diversity. The remaining locations were then processed using DigitalGlobe’s GeoHIVE crowdsourcing platform. Members of the GeoHIVE crowd were asked to validate the presence of categories in satellite images, as shown in Figure 9. The interface uses center-point location information to draw a circle around a possible object of interest. The interface then asks users to rapidly verify the existence of a particular label, as extracted from the VGI datasets, using the ‘1’, ‘2’, and ‘3’ keys to represent

existence, non-existence, and cloud cover.

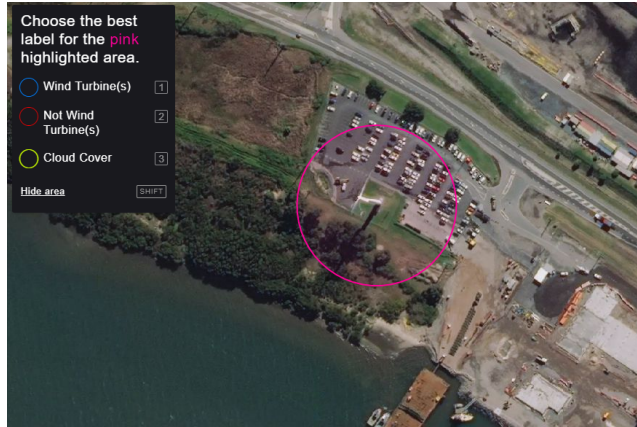


Figure 9: Sample image (“wind farm”) of what a GeoHIVE user might see while validating potential fMoW features. Instructions can be seen in the top-left corner that inform users to press the ‘1’, ‘2’, or ‘3’ keys to validate existence, non-existence, or cloud obscuration of a particular object.

For validation of object localization, a different interface is used that asks users to draw a bounding box around the object of interest after being given an initial seed point. The visualization for this is shown in Figure 10, and the seed point can be seen as a green dot located on the object of interest. Users are additionally provided some instructions regarding how large of a box to draw, which may vary by object class. This interface is more complex than the location selection interface, which is why it is performed after object existence can be confirmed and non-cloudy high-quality imagery is obtained. A smaller and more experienced group of users is also used for this task to help ensure the quality of the annotations.

Appendix III. Additional Results

Introduced in the main paper, CNN-I-1 and CNN-IM-1 make predictions for each individual view. All other methods repeat their prediction over the full sequence. Again, we note that these tests are clearly not fair to some categories, such as “construction site”, where some views may not even contain the category. However, we show results for these tests for completeness. Only the average values, which do not include “false detection” results, are shown in the main paper. We show per-category results in Table 4.

Appendix IV. Dataset Examples

Figure 11 shows one example for each category in our dataset. For viewing purposes, regions within the full image chip were extracted using the scaled bounding box coordinates for the categories. For the baseline approaches

Draw a rectangle around the Bus Station located in the center of this image.

Using your mouse, click and draw a rectangle over the "Bus Station" with your mouse.

Please do the following:

- Drag a box over the "Bus Station" closest to the small green circle.
- Make sure to include the feature in its entirety within your box, and that the box tightly fits the edges of the Bus Station.
- Provide feedback in the comment box below the image if there are issues or the "Bus Station" is not visible in the image.
- Press the spacebar key or click reset at the bottom of the image to remove your box.



Comment:

Reset Submit

(a) ground transportation station

Draw a rectangle around the Helicopter Heliport located in the center of this image.

Using your mouse, click and draw a rectangle over the "Helicopter Heliport" with your mouse.

Please do the following:

- Drag a box over the "Helicopter Heliport" closest to the small green circle.
- Make sure to include the feature in its entirety within your box, and that the box tightly fits the edges of the Helicopter Heliport.
- Provide feedback in the comment box below the image if there are issues or the "Helicopter Heliport" is not visible in the image.
- Press the spacebar key or click reset at the bottom of the image to remove your box.



Comment:

Reset Submit

(b) helipad

	CNN-I-1	CNN-I	LSTM-I	CNN-IM-1	CNN-IM	LSTM-IM
false_detection	0.662	0.737	0.732	0.825	0.840	0.821
airport	0.815	0.864	0.819	0.904	0.905	0.835
airport hangar	0.664	0.746	0.685	0.647	0.696	0.726
airport terminal	0.653	0.726	0.757	0.659	0.758	0.782
amusement park	0.698	0.751	0.736	0.852	0.901	0.846
aquaculture	0.642	0.743	0.767	0.752	0.798	0.790
archaeological site	0.458	0.532	0.507	0.531	0.624	0.622
barn	0.598	0.678	0.675	0.635	0.697	0.682
border checkpoint	0.232	0.268	0.311	0.367	0.465	0.497
burial site	0.736	0.788	0.802	0.750	0.821	0.830
car dealership	0.664	0.712	0.771	0.662	0.716	0.748
construction site	0.286	0.436	0.423	0.252	0.347	0.407
crop field	0.853	0.879	0.871	0.902	0.933	0.929
dam	0.755	0.805	0.778	0.785	0.839	0.861
debris or rubble	0.297	0.330	0.536	0.296	0.365	0.439
educational institution	0.461	0.517	0.482	0.537	0.585	0.601
electric substation	0.771	0.852	0.865	0.786	0.847	0.859
factory or powerplant	0.406	0.461	0.461	0.488	0.534	0.542
fire station	0.337	0.382	0.450	0.368	0.471	0.516
flooded road	0.253	0.254	0.240	0.553	0.634	0.809
fountain	0.659	0.744	0.720	0.749	0.811	0.857
gas station	0.691	0.779	0.806	0.704	0.767	0.785
golf course	0.852	0.906	0.926	0.895	0.932	0.898
ground transportation station	0.627	0.691	0.733	0.663	0.734	0.764
helipad	0.703	0.814	0.866	0.730	0.834	0.804
hospital	0.331	0.385	0.395	0.356	0.447	0.468
impooverished settlement	0.429	0.484	0.546	0.720	0.764	0.691
interchange	0.804	0.852	0.691	0.898	0.912	0.927
lake or pond	0.615	0.700	0.625	0.604	0.661	0.676
lighthouse	0.634	0.727	0.751	0.734	0.805	0.854
military facility	0.520	0.564	0.627	0.575	0.630	0.685
multi-unit residential	0.388	0.433	0.472	0.429	0.517	0.523
nuclear powerplant	0.548	0.575	0.759	0.588	0.650	0.494
office building	0.180	0.229	0.245	0.201	0.225	0.213
oil or gas facility	0.692	0.757	0.767	0.761	0.824	0.859
park	0.563	0.624	0.653	0.611	0.658	0.685
parking lot or garage	0.710	0.778	0.791	0.645	0.694	0.704
place of worship	0.560	0.637	0.642	0.631	0.703	0.729
police station	0.187	0.216	0.225	0.165	0.199	0.317
port	0.630	0.646	0.621	0.668	0.710	0.642
prison	0.540	0.614	0.657	0.596	0.656	0.729
race track	0.847	0.893	0.880	0.899	0.936	0.924
railway bridge	0.645	0.704	0.759	0.697	0.762	0.794
recreational facility	0.864	0.908	0.925	0.868	0.911	0.909
road bridge	0.667	0.712	0.728	0.710	0.742	0.758
runway	0.781	0.847	0.806	0.861	0.899	0.900
shipyard	0.388	0.416	0.326	0.397	0.390	0.411
shopping mall	0.549	0.617	0.622	0.589	0.676	0.675
single-unit residential	0.643	0.700	0.705	0.645	0.711	0.658
smokestack	0.665	0.756	0.762	0.673	0.792	0.782
solar farm	0.784	0.862	0.884	0.828	0.852	0.882
space facility	0.748	0.878	0.788	0.859	0.885	0.971
stadium	0.844	0.866	0.903	0.853	0.871	0.879
storage tank	0.895	0.933	0.920	0.895	0.930	0.921
surface mine	0.746	0.789	0.754	0.779	0.837	0.848
swimming pool	0.859	0.916	0.903	0.857	0.894	0.881
toll booth	0.841	0.874	0.878	0.918	0.949	0.947
tower	0.642	0.741	0.765	0.674	0.749	0.777
tunnel opening	0.789	0.852	0.880	0.914	0.943	0.932
waste disposal	0.475	0.562	0.516	0.478	0.583	0.632
water treatment facility	0.815	0.842	0.786	0.783	0.841	0.864
wind farm	0.899	0.932	0.934	0.928	0.950	0.972
zoo	0.471	0.531	0.563	0.552	0.606	0.637
Average	0.618	0.678	0.684	0.666	0.722	0.735

Figure 10: Sample images of the interface used to more precisely localize objects within an image. In each example, a green dot is placed near the center of the pertinent object. Users are able to draw a bounding box by clicking and dragging. Instructions at the top of each example inform the user how to use the interface and also provide any category-specific instructions that may be relevant. Comments regarding issues such as clouds or object misclassification can be entered near the bottom of the page before submitting an annotation.

presented in the main paper, smaller boxes were given more context than larger boxes, and therefore it may appear for some categories with smaller sizes (e.g., smoke stacks) that there is a lot more context than expected. It is important

Table 4: F1 scores for different approaches on an individual image basis. Color formatting was applied to each column independently. The average values shown at the bottom of the table are calculated without the false detection scores. CNN-I-1 and CNN-IM-1 make predictions for each individual view. All other methods repeat their prediction over the full sequence.

to keep in mind that the images for each category in the full dataset vary in quality, have different weather conditions (e.g., snow cover), contain drastically different context (e.g., desert vs. urban), have different levels of difficulty for recognition, and other variations.



Figure 11: One example per category in fMoW.

References

- [1] S. Abu-El-Haija, N. Kothari, J. Lee, P. Natsev, G. Toderici, B. Varadarajan, and S. Vijayanarasimhan. YouTube-8M: A Large-Scale Video Classification Benchmark. *arXiv preprint arXiv:1609.08675*, 2016.
- [2] S. Antol, A. Agrawal, J. Lu, M. Mitchell, D. Batra, C. Lawrence Zitnick, and D. Parikh. VQA: Visual Question Answering. In *ICCV*, 2015.
- [3] A. Chang, A. Dai, T. Funkhouser, M. Halber, M. Nießner, M. Savva, S. Song, A. Zeng, and Y. Zhang. Matterport3d: Learning from rgb-d data in indoor environments. *arXiv preprint arXiv:1709.06158*, 2017.
- [4] G. Cheng, J. Han, and X. Lu. Remote Sensing Image Scene Classification: Benchmark and State of the Art. *Proc. IEEE*, 2017.
- [5] N. DigitalGlobe, CosmiQ Works. Spacenet. *Dataset available from <https://aws.amazon.com/public-datasets/spacenet/>*, 2016.
- [6] J. Donahue, L. Anne Hendricks, S. Guadarrama, M. Rohrbach, S. Venugopalan, K. Saenko, and T. Darrell. Long-term Recurrent Convolutional Networks for Visual Recognition and Description. In *CVPR*, 2015.
- [7] M. Everingham, S. A. Eslami, L. Van Gool, C. K. Williams, J. Winn, and A. Zisserman. The Pascal Visual Object Classes Challenge: A Retrospective. *IJCV*, 2015.
- [8] L. Fei-Fei, R. Fergus, and P. Perona. One-Shot Learning of Object Categories. *PAMI*, 2006.
- [9] G. Griffin, A. Holub, and P. Perona. Caltech-256 Object Category Dataset. 2007.
- [10] D. Harwath and J. R. Glass. Learning Word-Like Units from Joint Audio-Visual Analysis. *ACL*, 2017.
- [11] K. He, X. Zhang, S. Ren, and J. Sun. Deep residual learning for image recognition. In *CVPR*, 2016.
- [12] G. Huang, Z. Liu, L. van der Maaten, and K. Q. Weinberger. Densely Connected Convolutional Networks. *CVPR*, 2017.
- [13] N. Jean, M. Burke, M. Xie, W. M. Davis, D. B. Lobell, and S. Ermon. Combining Satellite Imagery and Machine Learning to Predict Poverty. *Science*, 2016.
- [14] A. Karpathy and L. Fei-Fei. Deep Visual-Semantic Alignments for Generating Image Descriptions. In *CVPR*, 2015.
- [15] A. Karpathy, G. Toderici, S. Shetty, T. Leung, R. Suktanar, and L. Fei-Fei. Large-scale Video Classification with Convolutional Neural Networks. In *CVPR*, 2014.
- [16] D. Kingma and J. Ba. Adam: A Method for Stochastic Optimization. *ICLR*, 2014.
- [17] I. Krasin, T. Duerig, N. Alldrin, V. Ferrari, S. Abu-El-Haija, A. Kuznetsova, H. Rom, J. Uijlings, S. Popov, A. Veit, S. Belongie, V. Gomes, A. Gupta, C. Sun, G. Chechik, D. Cai, Z. Feng, D. Narayanan, and K. Murphy. Openimages: A public dataset for large-scale multi-label and multi-class image classification. *Dataset available from <https://github.com/openimages>*, 2017.
- [18] T.-Y. Lin, M. Maire, S. Belongie, J. Hays, P. Perona, D. Ramanan, P. Dollár, and C. L. Zitnick. Microsoft COCO: Common Objects in Context. In *ECCV*, 2014.
- [19] D. Marmanis, M. Datcu, T. Esch, and U. Stilla. Deep Learning Earth Observation Classification Using ImageNet Pretrained Networks. *GRSL*, 2016.
- [20] A. Miech, I. Laptev, and J. Sivic. Learnable pooling with Context Gating for video classification. *arXiv preprint arXiv:1706.06905*, 2017.
- [21] Y. Pan, T. Mei, T. Yao, H. Li, and Y. Rui. Jointly Modeling Embedding and Translation to Bridge Video and Language. In *CVPR*, 2016.
- [22] O. Russakovsky, J. Deng, H. Su, J. Krause, S. Satheesh, S. Ma, Z. Huang, A. Karpathy, A. Khosla, M. Bernstein, et al. Imagenet large scale visual recognition challenge. *IJCV*, 2015.
- [23] K. Simonyan and A. Zisserman. Very deep convolutional networks for large-scale image recognition. *arXiv preprint arXiv:1409.1556*, 2014.
- [24] K. Tang, M. Paluri, L. Fei-Fei, R. Fergus, and L. Bourdev. Improving Image Classification with Location Context. In *ICCV*, 2015.
- [25] S. Wang, M. Bai, G. Mattyus, H. Chu, W. Luo, B. Yang, J. Liang, J. Cheverie, S. Fidler, and R. Urtasun. Torontocity: Seeing the world with a million eyes. *ICCV*, 2017.
- [26] T. Weyand, I. Kostrikov, and J. Philbin. Planet-photo geolocation with convolutional neural networks. In *ECCV*, 2016.
- [27] G.-S. Xia, J. Hu, F. Hu, B. Shi, X. Bai, Y. Zhong, L. Zhang, and X. Lu. AID: A Benchmark Data Set for Performance Evaluation of Aerial Scene Classification. *TGRS*, 2017.
- [28] G.-S. Xia, X.-Y. Tong, F. Hu, Y. Zhong, M. Datcu, and L. Zhang. Exploiting deep features for remote sensing image retrieval: A systematic investigation. *arXiv preprint arXiv:1707.07321*, 2017.
- [29] Y. Yang and S. Newsam. Bag-Of-Visual-Words and Spatial Extensions for Land-Use Classification. In *ACM GIS*, 2010.
- [30] J. Yue-Hei Ng, M. Hausknecht, S. Vijayanarasimhan, O. Vinyals, R. Monga, and G. Toderici. Beyond Short

Snippets: Deep Networks for Video Classification. In *CVPR*, 2015.